

HST PanCET programme: a flat optical transmission spectrum for the Hot Jupiter WASP-101b

Alexander D. Rathcke ^{1,2★}, Lars A. Buchhave ¹, João M. Mendonça ¹, David K. Sing,³ Mercedes López-Morales,² Munazza K. Alam,⁴ Gregory W. Henry,⁵ Nikolay K. Nikolov ⁶, A. García Muñoz,⁷ Thomas Mikal-Evans ⁸, Hannah R. Wakeford,⁹ Leonardo A. Dos Santos ⁶ and Vinesh Maguire Rajpaul¹⁰

¹DTU Space, National Space Institute, Technical University of Denmark, Elektrovej 328, DK-2800 Kgs. Lyngby, Denmark

²Center for Astrophysics | Harvard & Smithsonian, 60 Garden Street, Cambridge, MA 02138, USA

³Department of Earth and Planetary Sciences, Johns Hopkins University, Baltimore, MD 21218, USA

⁴Carnegie Earth & Planets Laboratory, 5241 Broad Branch Road NW, Washington, DC 20015, USA

⁵Center of Excellence in Information Systems, Tennessee State University, Nashville, TN 30209, USA

⁶Space Telescope Science Institute, 3700 San Martin Drive, Baltimore, MD 21218, USA

⁷AIM, CEA, CNRS, Université Paris-Saclay, Université de Paris, F-91191 Gif-sur-Yvette, France

⁸Max Planck Institute for Astronomy, Königstuhl 17, D-69117 Heidelberg, Germany

⁹School of Physics, University of Bristol, HH Wills Physics Laboratory, Tyndall Avenue, Bristol BS8 1TL, UK

¹⁰Astrophysics Group, Cavendish Laboratory, University of Cambridge, Cambridge CB3 0HE, UK

Accepted 2023 March 28. Received 2023 March 23; in original form 2022 March 4

ABSTRACT

We present an optical transmission spectrum of the hot Jupiter WASP-101b. We observed three primary transits with *Hubble Space Telescope* (*HST*)/Space Telescope Imaging Spectrograph, covering a wavelength range from 0.3 to 1 μm . The observations suffer from significant systematics that we model using Gaussian Processes. Kernel selection for the Gaussian Processes is performed in a data-driven approach through Bayesian model comparison. We find a flat and featureless transmission spectrum, corroborating a previous measurement obtained with *HST*/Wide-Field Camera 3 in the 1–1.7 μm range. The spectrum is consistent with high-altitude clouds located at less than 100 μbar . This cloud layer completely blocks our view into deeper parts of the atmosphere and makes WASP-101b the cloudiest gas giant observed so far. We compute a series of temperature-pressure profiles for WASP-101b and compare these to condensation curves for cloud particles, which match clouds composed of silicates. We also include 13 transits observed with Transiting Exoplanet Survey Satellite and use these to refine system parameters.

Key words: methods: data analysis – methods: observational – planets and satellites: atmospheres – planets and satellites: gaseous planets.

1 INTRODUCTION

The study of exoplanetary atmospheres has progressed significantly since the first detection of an atmosphere just two decades ago (Charbonneau et al. 2002). Since then the most powerful space- and ground-based telescopes have provided a wealth of atmospheric observations, and this progress has now facilitated the first atmospheric population studies (e.g. Sing et al. 2016; Crossfield & Kreidberg 2017; Tsiaras et al. 2018). Due to their favourable signal strength, most of the planets studied in this way are thus far highly irradiated gas giants (hot Jupiters), which have revealed a great diversity in terms of atmospheric characteristics. While a variety of chemical species have been detected in these atmospheres, a key finding from around 20 yr of hot Jupiter atmospheric observations is that the presence of clouds and hazes appears to be very common (e.g. Wakeford et al. 2019). Using transmission spectroscopy, their

presence has been inferred from the muting of spectral features in the case of clouds and from the slope introduced in the blue part of the atmospheric spectrum in the case of hazes. Additionally, they have also been inferred from phase-curve observations through the differences in reflectivity across the planet’s disc (e.g. Demory et al. 2013; Garcia Munoz & Isaak 2015). While ubiquitous, their effect on the spectrum of individual atmospheres is highly varying. Some planets show signs of a mostly clear atmosphere (e.g. Nikolov et al. 2018; Alam et al. 2021), while others present us with a flat spectrum without any signs of spectral features (e.g. Gibson et al. 2013). Given the observed diversity, previous studies have found this varying muting effect to represent a continuum from clear to cloudy atmospheres for hot Jupiters (Sing et al. 2016; Barstow et al. 2017; Pinhas et al. 2019). By investigating the amplitude of the water absorption band at 1.4 μm for 14 planets, Stevenson (2016) found that the probability of clouds and hazes coincide with planetary temperature. Fu et al. (2017) expanded the sample size by another 20 planets and found that planets are decreasingly cloudy with

* E-mail: rathcke@space.dtu.dk

Table 1. *HST*/STIS observing information.

UT date	Visit #	Grating	Number of spectra	Exp. time (s)
2017-04-24	62	G430L	48	253
2017-08-24	61	G430L	48	253
2017-11-07	63	G750L	72	161

increasing equilibrium temperature up to 1100 K, then increasingly cloudy with increasing temperature between 1100 and 1600 K, and finally decreasingly cloudy with increasing temperature up to 2300 K. In this paper, we investigate the atmosphere of the hot Jupiter WASP-101b ($T_{\text{eq}} \sim 1550$ K) and add it to the context described above.

WASP-101b was discovered in 2013 by WASP-South (Hellier et al. 2014) and is an inflated hot Jupiter with $R = 1.41 \pm 0.05 R_J$ and $M = 0.5 \pm 0.04 M_J$ (Hellier et al. 2014), yielding a mean density of $\rho = 0.24 \pm 0.03 \text{ g cm}^{-3}$ and a surface gravity of $g = 6.2 \text{ m s}^{-2}$. Its host star is of spectral-type F6 with apparent magnitude $V = 10.3$ mag and is located in the constellation Canis Major with a precise location of RA = $06^{\text{h}}33^{\text{m}}24^{\text{s}}.0$, Dec. = $-23^{\circ}29'10''$. With a semimajor axis of $a = 0.05$ au, it orbits its host star with a period $P = 3.59$ d, corresponding to an equilibrium temperature of ~ 1550 K. A previous study of the planet in the Near-Infrared (NIR) using Wide-Field Camera 3 (WFC3) mounted on the *Hubble Space Telescope* (*HST*) found that the planet exhibits an absence of water vapour as well as the absence of a clear atmosphere at a confidence level of 13σ (Wakeford et al. 2017). Here, we expand upon the findings of Wakeford et al. (2017) by including observations in the optical to get a better understanding of the cloud properties of WASP-101b. The paper is structured as follows: Section 2 describes the observations and how the data are reduced, in Section 3 we present our analysis procedure and the resulting light curves. We then go on to discuss the implications of the results in Section 4, and conclude in Section 5.

2 OBSERVATIONS AND DATA REDUCTION

2.1 Observations

We analyse data obtained as part of the Panchromatic Comparative Exoplanetary Treasury (PanCET) programme (PIs: Sing & López-Morales, Cycle 24, GO 14767). In total, we observed three primary transits of WASP-101b with the Space Telescope Imaging Spectrograph (STIS) installed on *HST*. Two of these transits were observed using the G430L grating, while the last was observed with the G750L grating. The G430L grating covers a wavelength range from 0.29 to $0.57 \mu\text{m}$, while the G750L grating covers the range from 0.53 to $1.03 \mu\text{m}$. With a resolving power of ~ 2.7 and $\sim 4.9 \text{ \AA}$ per pixel the two gratings provide resolutions of $\lambda/\Delta\lambda \sim 500\text{--}1000$.

Each transit event was observed during five *HST* orbits. *HST* orbits the Earth once every ~ 95 min, of which data collection is halted for ~ 45 min when *HST* is occulted by the Earth. For each transit event, this strategy resulted in 5 chunks of ~ 50 min time-series data separated by ~ 45 min gaps with no science data collection. In total, this lead to 48–72 spectra obtained during each planetary transit. Observations were carried out with the 52×2 arcsec² slit to minimize slit losses and readout times were reduced by only reading out a smaller 1024×128 pixel part of the CCD. With careful treatment of instrumental systematics, this approach has previously been shown to allow almost Poisson limited signal-to-noise ratio (SNR) during transits (e.g. Huitson et al. 2012; Sing et al. 2013). See Table 1 for the specific observing information.

2.2 Cosmic ray correction, data reduction, and spectral extraction

We now turn to the preparation of the data for further analysis. As the procedure we use is identical to the one performed in Rathcke et al. (2021) for a similar data set, we only briefly explain it here and refer readers interested in the details to our previous work. The long duration of the exposures results in several cosmic ray hits on the data frames. The CALSTIS¹ pipeline does not remove all of them to a sufficient degree and we, therefore, utilize the time-series nature of our data to correct for this. Similar to the method described in Nikolov et al. (2014), we do this by using a difference image approach, where we compare frames with their neighbours in time to find and replace pixels that have count variations exceeding a 4σ threshold. The data reduction is performed uniformly using CALSTIS v3.4 to bias-, flat- and dark-correct the data before extracting 1D spectra using IRAFs APALL procedure. The APALL procedure is run with an aperture of width 13, as we find this to provide the lowest photometric scatter in the out-of-transit data. Additionally, we choose to use APALL with no background subtraction as previous work has shown it to minimize residual scatter (Sing et al. 2011; Nikolov et al. 2015). Finally, we map our spectra on to a wavelength solution obtained from the corresponding .x1d files.

3 ANALYSIS

As with the spectral extraction, the analysis procedure also follows that of Rathcke et al. (2021). We again briefly explain our approach but refer interested readers to Rathcke et al. (2021) for a detailed explanation of all the steps.

3.1 Analysis procedure

We use a fully Bayesian framework that allows us to simultaneously model the light curves and account for systematics in our data. To do this, we treat each light curve as a Gaussian Process (GP) and sample using nested sampling. GPs is a powerful modelling tool with widespread applications. In more recent years, they have been adapted by the exoplanet community where they are commonly used to model stellar activity in radial velocity data (e.g. Rajpaul et al. 2015; Jones et al. 2017) and instrumental systematics in transmission spectroscopy studies (e.g. Gibson et al. 2012; Evans et al. 2018). For a more general introduction to GPs, we refer to Rasmussen & Williams (2006). Specifically, we developed our analysis framework in PYTHON using the GP package GEORGE (Ambikasaran et al. 2015), and we implement nested sampling via PYMULTINEST (Buchner et al. 2014), which utilizes the underlying MULTINEST (Feroz & Hobson 2008; Feroz, Hobson & Bridges 2009; Feroz et al. 2019) code. To model the light curve, we use the analytical transit model of Mandel & Agol (2002) as the mean function of the GP. This analytical model is a function of the mid-transit times, the orbital period, the planet-to-star radius ratio, the semimajor axis, the orbital inclination, and the coefficients describing the limb darkening effect. The transit model is implemented by using the BATMAN PYTHON package (Kreidberg 2015), and we account for limb darkening by using the non-linear four-parameter function (Claret 2003), where we fix the four parameters in our fits to values calculated using limb darkening toolkit(LDtk; Parviainen & Aigrain 2015).

¹CALSTIS is a collection of software built in the IRAF environment for the purpose of STIS data calibration (Katsanis & McGrath 1998).

3.2 Kernel selection by model comparison

In addition to the mean function, a GP is defined by a kernel function. In our case, the mean function models the function of interest, while the kernel simultaneously model systematics that could be either instrumental or astrophysical in nature. In contrast to the analytic model describing the transit, we do not have any parametric function to describe the systematics. One of the advantages of using GPs is that it provides a non-parametric approach that determines a distribution over possible functions that are consistent with the observations rather than estimating a distribution over parameters. The kernel function can take many forms of various complexity, and we need to choose a kernel function that best matches the actual systematics we are trying to model. To do this our Bayesian framework comes in handy since the nested sampling provides us with the marginal likelihood (or evidence) of a given model allowing us to directly perform model comparison by comparing the evidences. In other words, it provides a direct way of comparing the performance between choices of kernel functions and thus determines which kernel is most appropriate to model the systematics. Using the nested sampling framework, we conduct a search for an optimal choice of kernel. This search is performed on the white light curve, and we do this by using time as our input vector and individually testing a suite of the following five commonly used kernels:

(i) Squared exponential:

$$k(x_n, x_m) = \sigma^2 \exp\left(-\frac{(x_n - x_m)^2}{2\ell^2}\right). \quad (1)$$

(ii) Rational quadratic:

$$k(x_n, x_m) = \sigma^2 \left(1 + \frac{(x_n - x_m)^2}{2\alpha\ell^2}\right)^{-\alpha}. \quad (2)$$

(iii) Matérn 3/2:

$$k(x_n, x_m) = \sigma^2 \left(1 + \frac{\sqrt{3}|x_n - x_m|}{\ell}\right) \times \exp\left(-\frac{\sqrt{3}|x_n - x_m|}{\ell}\right). \quad (3)$$

(iv) Periodic:

$$k(x_n, x_m) = \sigma^2 \exp\left(-\frac{2\sin^2(\pi|x_n - x_m|/p)}{\ell^2}\right). \quad (4)$$

(v) Linear:

$$k(x_n, x_m) = \sigma^2 (x_n - c)(x_m - c). \quad (5)$$

Here, x_n, x_m correspond to the elements in the covariance matrix, σ is the amplitude parameter describing the maximum variance allowed, ℓ is the length-scale parameter, α is the Gamma distribution parameter, p defines the period between repetitions in the periodic kernel, and c is a constant term. Besides the above five kernels, we also incorporate a white noise kernel in all our fits of the form:

$$\text{White Noise: } k(x_n, x_m) = \sigma_{wn}^2 \delta(x_n, x_m), \quad (6)$$

where σ_{wn} is the white noise amplitude (in our case the photon noise) for each data point, and $\delta(x_n, x_m)$ is the Kronecker delta function.

Any additive or multiplicative combination of the above kernels is still a valid kernel, and we use this to expand our search for an optimal kernel function by systematically trying all two-component additive and multiplicative combinations of our five chosen ‘standard’ kernels. Following this step, we once again allow an additional kernel

to be added or multiplied on to the two-component kernels, thus forming a three-component kernel, and once again comparing the performance based on the evidence. We find that a three-component kernel is favoured by the data and that introducing a fourth component worsens the evidence, indicative of our model starting to overfit. As in Rathcke et al. (2021), we find that the data itself favours a kernel of the form:

$$k(x_n, x_m) = \sigma_a^2 \exp\left(-\frac{2\sin^2(\pi|x_n - x_m|/p)}{\ell_a^2}\right) \exp\left(-\frac{|x_n - x_m|^2}{2\ell_b^2}\right) + \sigma_b^2 \left(1 + \frac{\sqrt{3}|x_n - x_m|}{\ell_c}\right) \exp\left(-\frac{\sqrt{3}|x_n - x_m|}{\ell_c}\right) + \sigma_{wn}^2 \delta(x_n, x_m), \quad (7)$$

where σ_a, σ_b are the allowed amplitudes, and ℓ_a, ℓ_b, ℓ_c are the correlation length-scales on which the model is allowed to vary.

While the above kernel is favoured by the data, we remark that a range of other kernels also results in relatively high Bayesian evidences. This indicates that our model selection is mainly able to reject inferior kernels, but is less sensitive to the exact choice of kernel from among the best-performing ones. This is underscored by the best-performing composite kernels producing consistent transmission spectra. We use equation (7) as our kernel in this work, but note that future work could perform model averaging, such that multiple competing kernels supported by the data would drive the atmospheric inferences. This would mean that inferences would account for model uncertainty and not just parameter uncertainty.

3.3 White light-curve fits

The determination of the used composite kernel for the GP is found by performing fits of the white light curves, which are the summation of the entire dispersion axis. With the exception of the limb darkening parameters, we allow all the parameters of the analytical transit model to vary together with the hyperparameters (amplitudes and length-scales) of the GP. In accordance with common practice, we discard all exposures from the first *HST* orbit and the first exposure of each subsequent orbit as they are known to suffer from unique and complex systematics arising from the telescope thermally relaxing into its new pointing position (Brown et al. 2001). We conduct the white light-curve fit jointly for the two G430L grating visits, but separately from the G750L grating visit. For all the parameters of the analytical transit model, we apply broad uniform priors corresponding to $\pm 20\sigma$ from the Transiting Exoplanet Survey Satellite (TESS) inferred values (see Section 3.5). The GP kernel length-scale hyperparameters are only limited to be between zero and the duration between the first and last observation, while the GP amplitude hyperparameters are limited to not be larger than the difference between the lowest and highest flux measurement. While the fits presented in this work uses uniform priors on the GP hyperparameters, we find that using a Jeffreys prior yield consistent results. These fits are visualized in Fig. 1.

3.4 Transmission spectrum fits

We assemble the transmission spectrum by fitting light curves produced by dividing the dispersion axis into spectrophotometric channels. To decide on how to bin the spectra, we enforce that each bin should have a signal-to-noise ratio (SNR) of around 1500 and that the edges of each bin should not coincide with strong spectral lines. This choice ensures that each bin is not dominated by photon noise, while still conserving most of the information from the transmission spectrum. As an exception to this binning scheme, we also construct

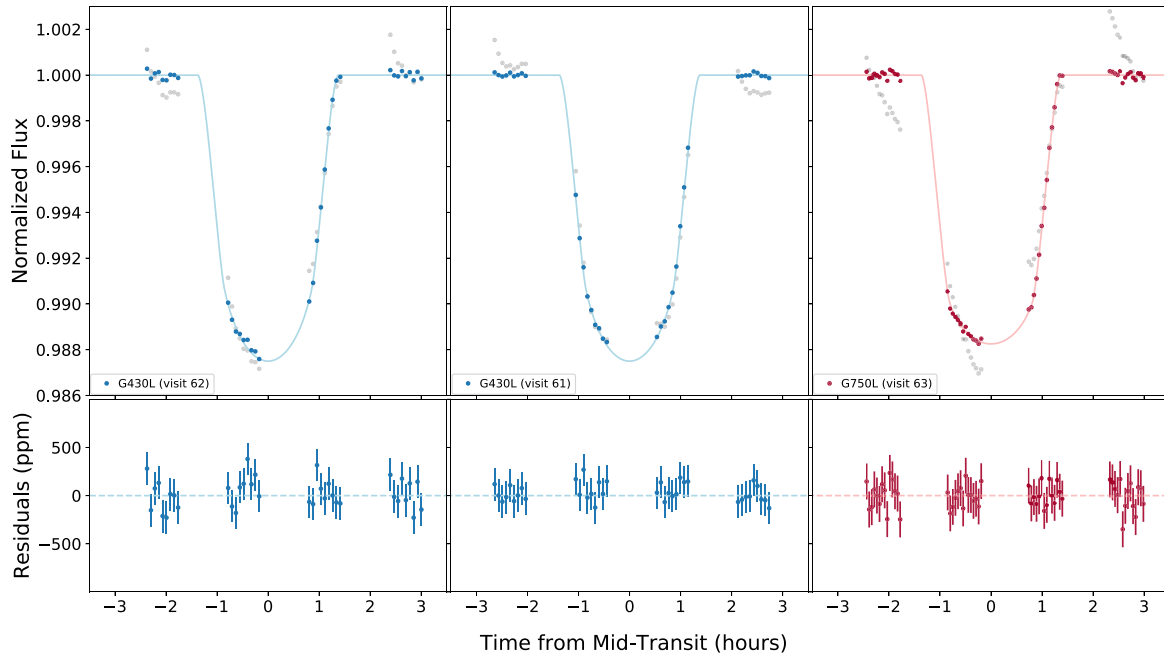


Figure 1. WASP-101b *HST*/STIS normalized white light curves from the data obtained during the 3 visits (left to right): visit 62 (G430L), visit 61 (G430L), and visit 63 (G750L). Top row: Data points after removing the systematic effects inferred from the GP analyses (blue and red points for the G430L and G750L gratings, respectively), with the best-fitting model (solid lines) and the raw light-curve data points prior to the GP analyses (transparent grey points). Bottom row: Corresponding O-C residuals, with photon noise error bars.

Table 2. System parameter results.

	a/R_*	Inclination ($^\circ$)
G430L white light fit	8.41 ± 0.10	85.084 ± 0.109
G750L white light fit	8.32 ± 0.12	84.918 ± 0.127
TESS	8.35 ± 0.09	84.934 ± 0.101
Weighted average	8.36 ± 0.06	84.981 ± 0.064

two narrower bins centred on the Na doublet (5890 Å, 5896 Å) and the K doublet (7665 Å, 7699 Å) to probe for the presence of the narrow-line cores of these alkali metals. With the spectrum divided into 26 bins, we then fix all the wavelength-independent parameters to the weighted average values quoted in Table 2 and run our fits by effectively only allowing R_p/R_* and the hyperparameters of the GP kernel to vary.

While the G430L and G750L gratings probe different wavelength regions, they do have an overlapping region between 0.53 and 0.57 μm . We use this overlap to correct for any systematic offset between the absolute transit depths of the two gratings by running additional fits in the overlapping region range for both gratings. We then use the difference in the median fitted R_p/R_* values from the two fits to uniformly offset the G430L portion of the transmission spectrum to match that of the G750L grating. Moreover, TESS observed WASP-101b for a total of 12 transits yielding tight constraints on R_p/R_* . To put the transmission spectrum on an absolute scale, we then use the same approach and run a fit for the G750L data that corresponds to the TESS bandpass and offset the entire STIS transmission spectrum with respect to the difference between the TESS transit depth and the G750L transit depth in the same bandpass. We find an offset of 1 per cent between the two STIS gratings and 0.5 per cent between STIS and TESS. The detrended binned light curves for all three visits are shown in Fig. 2 for visits 62 and 61 and Fig. 3 for visit 63. Our

final stitching-corrected transmission spectrum is printed in Table A1 and presented visually in Fig. 4.

A visual inspection of the transmission spectrum shows no obvious signs of absorption from the commonly found alkali metals sodium or potassium. Neither does it show any signs of a scattering slope or other absorbers and is thus one of the ‘flattest’ transmission spectra found to date. To emphasize how flat our resulting transmission spectrum is, we also include two cloud-free models with solar metallicity in Fig. 4 for reference.

3.5 TESS

In addition to the *HST* data, we include a broad-band (0.6–1.0 μm) TESS point to complement the transmission spectrum as well as to put the STIS transmission spectrum on an absolute scale. TESS observed five transits of WASP-101b in sector 6 (December 2018 to January 2019) and another eight transits in sector 33 (December 2020 to January 2021). To infer the TESS transit depth we use the two-minute cadence Presearch Data Conditioning light curves, which have already been corrected for instrumental systematics (Jenkins et al. 2016), followed by the removal of all data points that are marked by a corresponding quality flag. We discard the first transit from sector 33, as it is only a partial transit and fit the remaining 12 transits individually by extracting a 700 data-point window centred in the middle of each transit. This window size corresponds to roughly 23 h and thus supplies plenty of out-of-transit baseline. To carry out the fits, we use the analytical transit model of Mandel & Agol (2002) implemented via the PYTHON package BATMAN (Kreidberg 2015) as well as a linear trend in time and sample using the nested sampling algorithm implemented in the PYTHON package ULTRANEST (Buchner 2021). We account for limb darkening by using the non-linear four-parameter function (Claret 2003) and fix these to values found using LDtk (Parviainen & Aigrain 2015). We obtain a

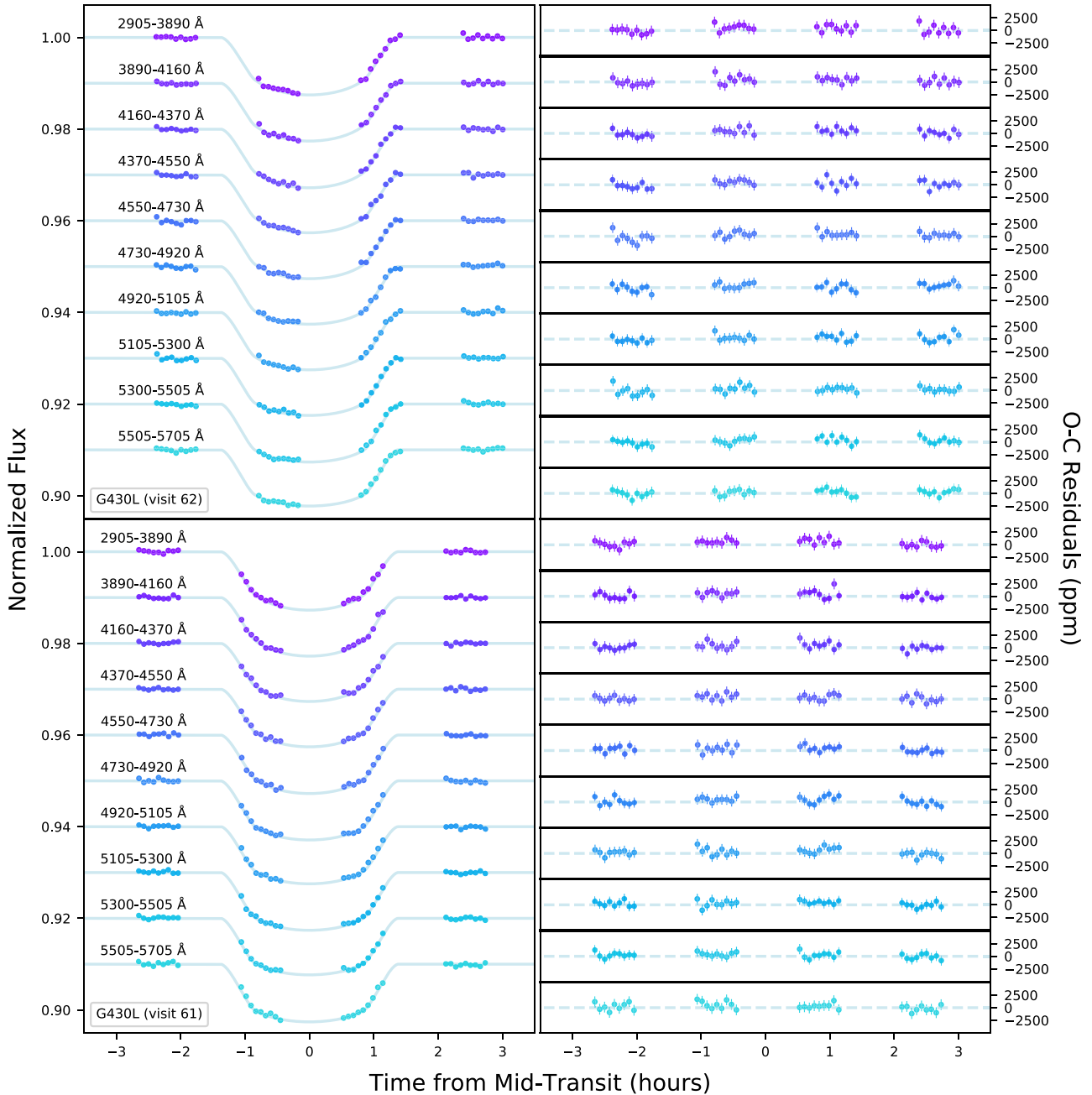


Figure 2. WASP-101b *HST/STIS* observations obtained with the G430L grating during visits 62 (top) and 61 (bottom). Left: Detrended light curves (points) and best-fitting transit models (solid lines). The light curves are vertically offset for clarity and are ordered with the bluest bin on top and the reddest bin on bottom. Right-hand panel: Corresponding O-C residuals in parts per million.

weighted average with 1σ uncertainties for the inclination = $84.934^\circ \pm 0.101^\circ$, a semimajor axis of $a/R_\star = 8.347 \pm 0.089$, and a planetary radius $R_p/R_\star = 0.10946 \pm 0.00024$. We visualize the inferred R_p/R_\star values for each of the 12 transits in Fig. 5 together with the weighted average and uncertainty.

3.6 Assessing stellar activity

Here, we investigate if there are signs of stellar activity possibly affecting the transmission spectrum that we need to correct for. To this end, we acquired 248 good nightly photometric observations (excluding occasional transit observations) of WASP-101 during

the five observing seasons 2017–18 through 2021–22 with the Tennessee State University Celestron 14-inch (C14) automated imaging telescope (AIT) located at Fairborn Observatory in southern Arizona (see e.g. Henry 1999; Eaton, Henry & Fekel 2003). The observations were made through a Cousins *R* filter with an SBIG STL-1001E CCD camera. Each nightly observation consists of 3–5 consecutive exposures of the WASP-101 field of view. The individual frames are co-added and reduced to differential magnitudes in the sense WASP-101 minus the mean brightness of six constant comparison stars in the same field. Further details of our observing, reduction, and analysis procedures can be found in Sing et al. (2015).

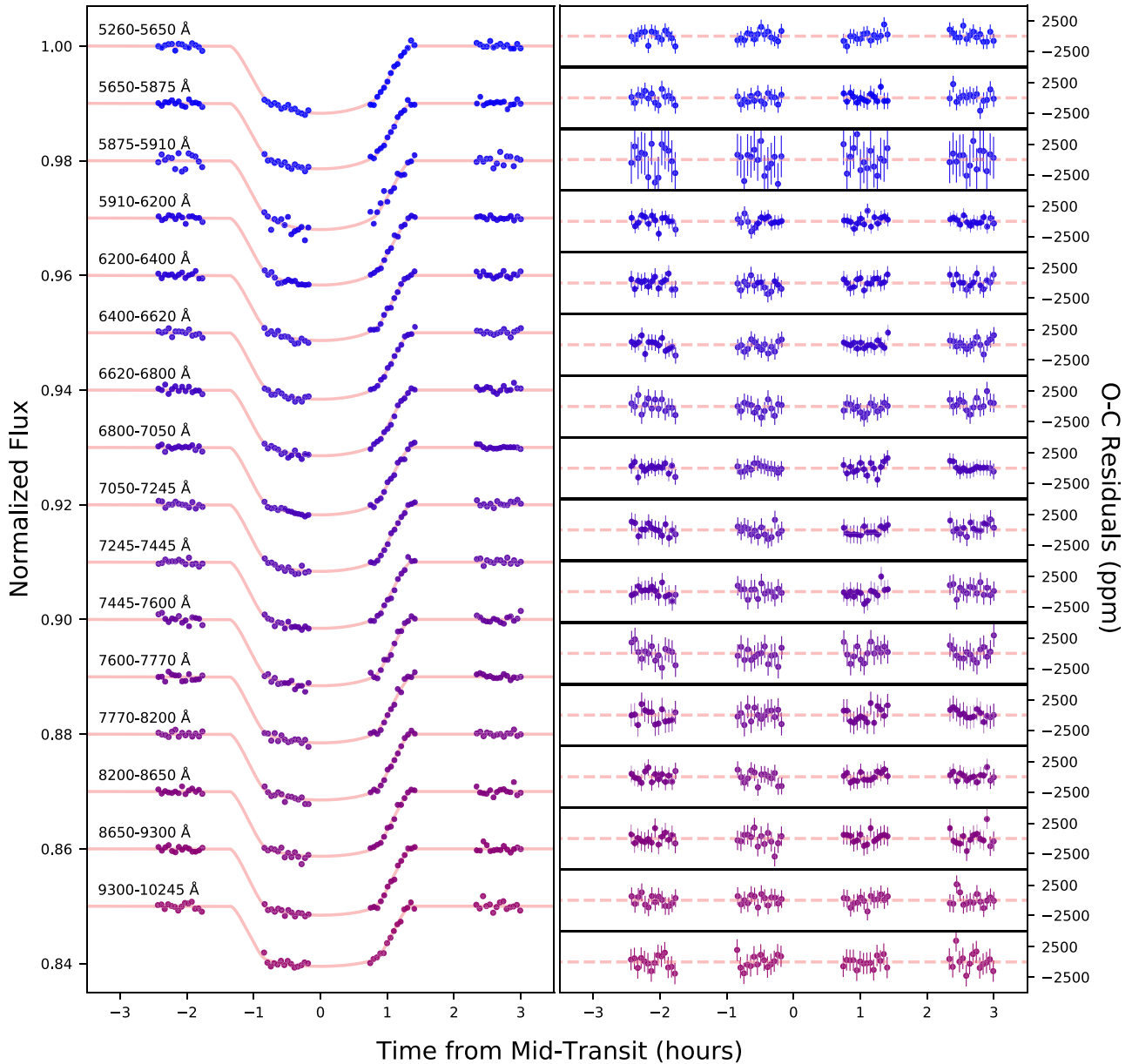


Figure 3. Same as Fig. 2, but for visit 63 observed with the G750L grating.

The observations are summarized by season in Table 3. Due to the star’s southerly declination of -23° , the observations were made at high airmass between 1.7 and 3.3, thus compromising their precision somewhat. The standard deviations of the individual observations from their respective seasonal means are given in column 4 of Table 3. The average for the five seasons is 0.003 86 mag, roughly 0.001 mag higher than C14’s typical precision. No significant periodicity is found in any of the individual observing seasons nor in the complete data set.

The nightly observations and seasonal mean magnitudes are plotted in Fig. 6 as small and large filled circles, respectively. The standard deviations of the seasonal means are somewhat larger than the size of the plot symbol, indicating there is very little or no measurable variability in the seasonal means. Considering that we find no evidence for significant variability, we are confident to proceed with performing inferences about the planetary atmosphere without performing any corrections for stellar activity.

4 DISCUSSION

In this section, we compare our obtained transmission spectrum with theoretical models in order to examine what information can be extracted from the inferred flat transmission spectrum. As the flat transmission spectrum suggests a high-altitude cloud deck obscuring the atmosphere, we explore the possible composition of the clouds. Finally, we use this section to put WASP-101b in context by comparing it to similar planets.

4.1 Retrieval with PLATON

While intuition suggests the flat transmission spectrum to be dominated by a high-altitude cloud layer, we run the PLATON² retrieval

²The PLATON documentation is available at: <https://platon.readthedocs.io>

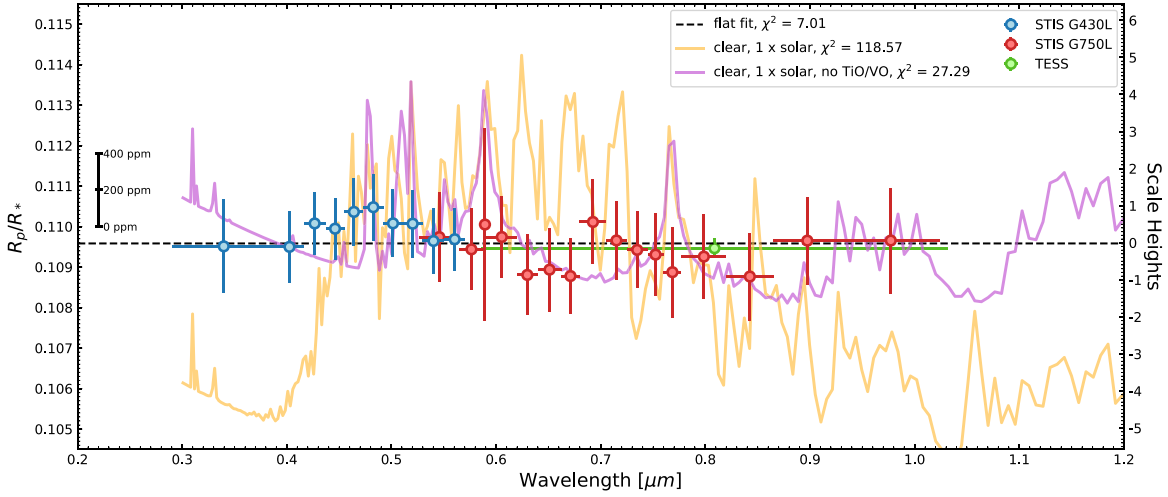


Figure 4. The inferred *HST/STIS* transmission spectrum of WASP-101b (blue and red circles for G430L and G750L gratings, respectively). The error bars represent the spectrophotometric bin size (horizontal) and the 1σ uncertainties obtained from the posterior samples (vertical). Additionally, we include the TESS transit depth (green circle). We also compare the observed transmission spectrum to cloud-free forward models computed with PLATON. The two models have solar metallicity, where one model includes absorption by TiO and VO (orange) while these two absorbers are excluded in the other (purple). The black dashed line is a linear fit included for reference. A scale marking corresponding transit depths in parts per million is inserted to the left of the data.

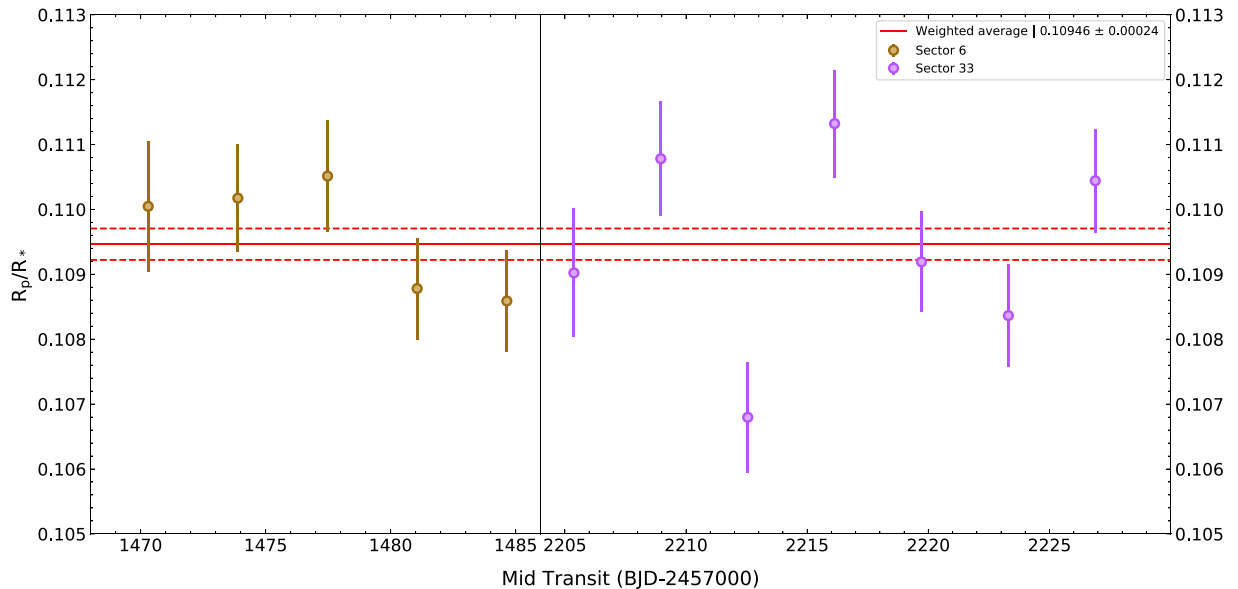


Figure 5. Individual transit depths for the 12 transits observed with TESS. The left-hand panel shows the five transits observed in Sector 6 (brown circles), while the right-hand panel shows the seven transits observed in Sector 33 (purple circles). Notice the ~ 2 -yr gap between the two sectors. The red lines denote the weighted average and the corresponding 1σ uncertainties.

Table 3. Summary of C14 AIT photometry of WASP-101.

Observing Season	N_{obs}	Date range (HJD – 2400 000)	Sigma (mag)	Seasonal mean (mag)
2017–18	31	58172–58229	0.00352	–2.13607
2018–19	59	58384–58591	0.00370	–2.13906
2019–20	55	58756–58956	0.00373	–2.13945
2020–21	68	59108–59327	0.00459	–2.13770
2021–22	35	59467–59630	0.00376	–2.13819

code (Zhang et al. 2020) to check if any information could be extracted from the transmission spectrum. PLATON is a PYTHON package that allows the retrieval of atmospheric characteristics. It assumes an isothermal temperature–pressure (T/P) profile and equilibrium chemistry but offers a wide range of temperatures, metallicities, C/O ratios, cloud-top pressures, and scattering slopes. Additionally, it allows for rainout, meaning that species that condensate at the given temperature will be assumed to sink deep into the atmosphere and be depleted at the pressure levels probed by transmission spectroscopy. In addition to the STIS data, we also include the TESS data point as well as the WFC3 data from Wakeford et al. (2017) in our retrievals.

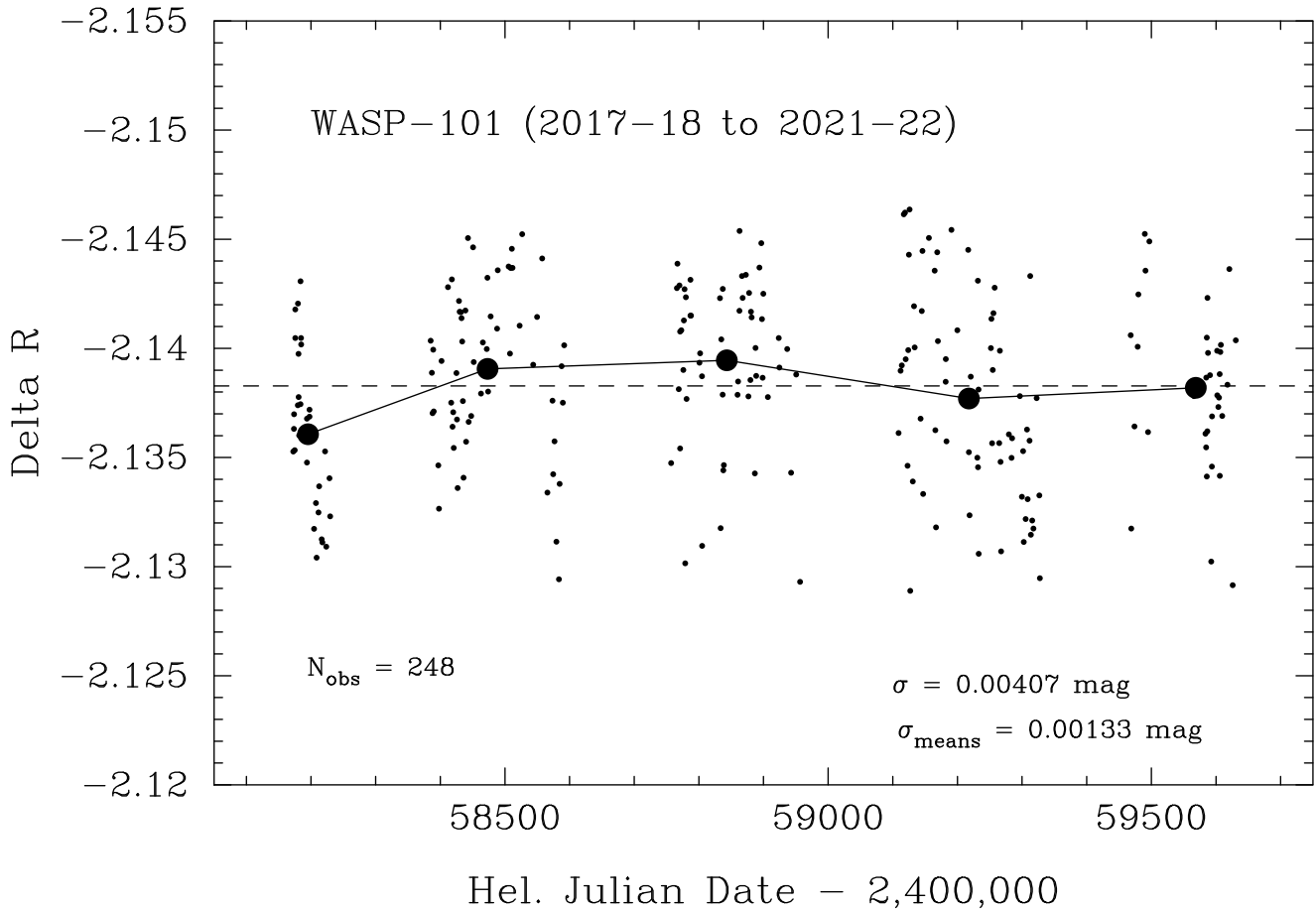


Figure 6. Cousins R -band photometry of WASP-101 from the five observing seasons 2017–18 through 2021–22 (small circles), acquired with the C14 automated imaging telescope (AIT) at Fairborn Observatory. The star is constant from night to night within each observing season to the limit of our precision. The seasonal mean magnitudes are plotted as large filled circles and cover a range of 0.0034 mag (see Table 3). These small changes in the yearly means are roughly consistent with the standard deviation of the seasonal means (0.001 33 mag).

Since we want to combine data obtained with different instruments and set-ups, we take care by not assuming the absolute transit depths. This is especially important when including the WFC3 data from Wakeford et al. (2017), as they used slightly different orbital parameters in their reduction of the transmission spectrum as well as using a ‘common-mode’ correction that removes any absolute baseline information. Even though we have already stitched the transmission spectrum for the two STIS gratings together using the overlapping region, we note that the fits carried out in the overlapping region also come with uncertainties and we therefore also want to take this into consideration.

To account for uncertainties when stitching the spectra, we modify the PLATON code to allow for offsets between the different data sets. Specifically, we use the G750L part of the transmission spectrum as a reference and allow the G430L and the WFC3 data to be uniformly offset with respect to the G750L part of the transmission spectrum. We also modify the PLATON code to sample using PYMULTINEST.

We then run three separate retrievals: one where we allow a grey cloud cover; another where we invoke hazes (we do this by setting the haze enhancement factor = 1100, see e.g. Goyal et al. 2019 for details); and a third where we assume the atmosphere is clear down to the 1 bar pressure level. Common between the three cases is that we initialize our retrieval by assuming uniform priors on the

temperature between 800 and 2200 K, a C/O ratio between 0.05 and 2, a metallicity between 0.1 and $1000\times$ solar, and an allowed offset of ± 5 per cent. For the two non-clear atmosphere cases, we disregard the degeneracy between the planetary radius and cloud-top pressure by fixing the planetary radius in our fits and initialize those two cases with allowed cloud-top pressure ranging from 1 μ bar to 1 bar. In the clear atmosphere case, we fix the cloud-top pressure at 1 bar and, instead, allow the radius of the planet to vary so as not to disfavour this fit if the fixed planetary radius should be slightly off.

In all three cases, a uniform offset of -1 per cent for the G430L data and $+2$ per cent for the WFC3 data is favoured (with respect to the G750L data). Because the retrieval is not able to adjust the cloud-top pressure for the clear atmosphere, the retrieval instead invokes a very high metallicity to compensate since this effectively compresses the atmosphere and hence flattens the transmission spectrum. Specifically, the metallicity converges towards the upper bound of the prior ($1000\times$ solar), which is the maximum value PLATON allows. In the two non-clear atmosphere cases the posteriors suggest cloud-top pressures at less than 100 μ bar. All three cases result in inferred temperatures of 1200–1300 K, which is slightly lower than the ~ 1550 K equilibrium temperature of the planet. The retrieval of temperatures colder than the equilibrium temperature is a known effect in 1D atmospheric retrieval approaches and arises when 1D averaged profiles are used to fit atmospheres that in reality will have

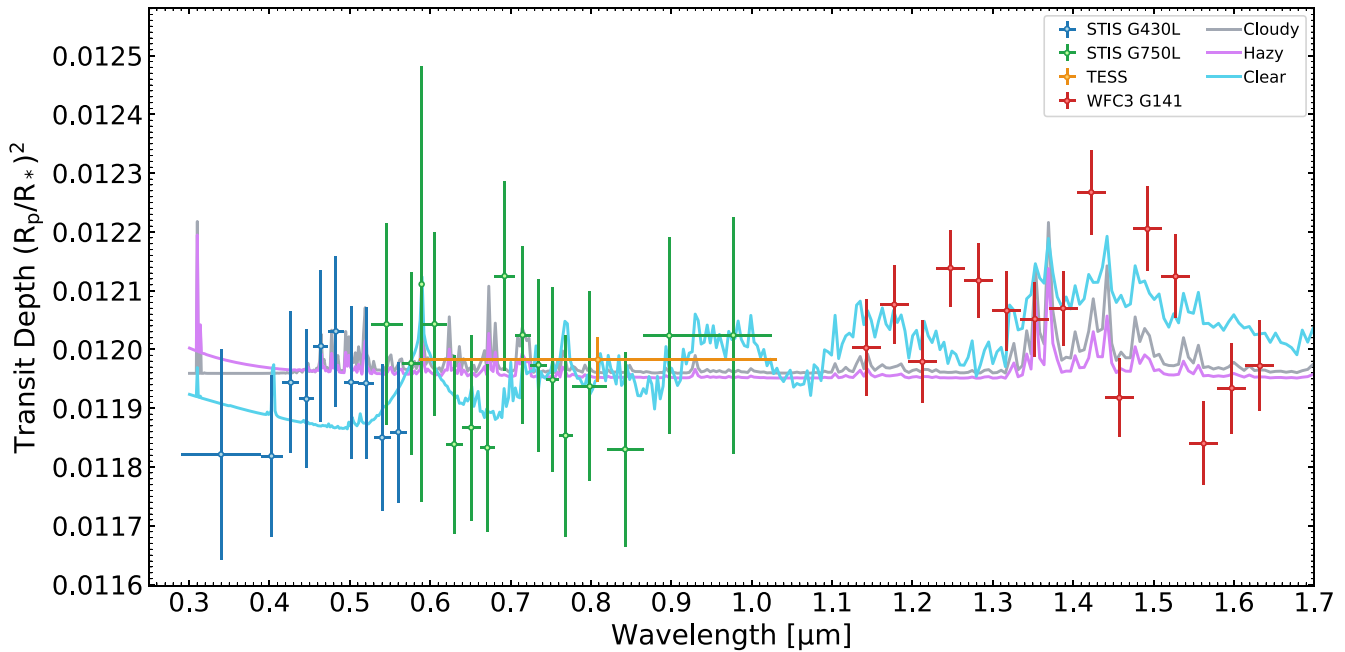


Figure 7. Atmospheric retrieval results of the transmission spectrum of WASP-101b. The retrieved models are found using PLATON (Zhang et al. 2020) and constitute three different cases: a cloudy atmosphere (grey), a hazy atmosphere (pink), and a clear atmosphere (blue). Overlaid are the combined observed transmission spectrum uniformly offset by -1 and $+2$ percent with respect to the G750L points for the G430L and WFC3 points, respectively.

different morning and evening terminator compositions (MacDonald, Goyal & Lewis 2020).

To evaluate the goodness of fit we use the Bayesian evidence ratios between the three retrievals and map them into an equivalent sigma value. We find that the cloudy case is strongly favoured by 3.9σ over the clear case, but only slightly favoured over the hazy case by 1.7σ . We visualize the resulting models from the three retrievals in Fig. 7. We note that the applied offsets to the G430L and WFC3 data shown in the figure correspond to the values found in the cloudy case.

4.2 Clouds

The sulphuric acid clouds in the Venusian atmosphere, the familiar water clouds known from Earth, and the ammonia, water, and ammonium hydrosulphide clouds in Jupiter demonstrate that clouds are omnipresent in the Solar system and come in a wide range of flavours. Likewise, observations have revealed that clouds are present in the vast majority of exoplanetary atmospheres. Specifically, it has been found that most hot Jupiters have clouds and/or hazes in the atmospheres to some extent (Sing et al. 2016). Wakeford et al. (2019) further investigated a sample of 37 hot Jupiter observations using *HST*/WFC3 and found that the water feature probed in that wavelength range is on average muted to 33 percent compared to the amplitude expected in a clear atmosphere. While the Solar system does not host any hot Jupiters, theoretical work suggests that the temperatures in hot Jupiters allow for exotic clouds not seen anywhere in the Solar system. By including the short wavelength coverage offered by STIS, we find no evidence for a scattering slope, and our retrieval using PLATON best describes the transmission spectrum by invoking high-altitude clouds. However, the information content in such a flat transmission spectrum does not directly offer clues to the formation and composition of such clouds, but a substantial body of theoretical work investigating this exists in the literature (e.g. Ackerman & Marley 2001; Helling, Woitke &

Thi 2008; Powell et al. 2018; Gao et al. 2020). To speculate on the composition of the cloud particles, we can compare temperature-pressure (T/P) profiles of WASP-101b with condensation curves for a range of proposed cloud particles. To do this, we start by computing a set of T/P profiles under various atmospheric assumptions.

4.2.1 Computing T/P profiles

The temperature structure of a planet’s atmosphere is mainly driven by the energy balance between the radiative and convective processes. The radiative processes include the deposition of stellar energy in the planet’s atmosphere and atmospheric thermal cooling. We adopt the 1D radiative-convective model described in Mendonça & Buchhave (2020) to work under WASP-101b-like conditions. To represent the radiative processes, the model uses a two-stream formulation as explained in Mendonça et al. (2015), which includes the effect of multiple scattering. A simple convection adjustment scheme represents convection. This scheme mixes the enthalpy instantaneously in a buoyant unstable atmospheric region (Mendonça et al. 2018 and Malik et al. 2019). The model uses k -distribution tables and integrates the radiative fluxes over 300 spectral bands and 20 Gaussian points, which has been shown by Malik et al. (2017) to be a robust spectral resolution for hot Jupiter simulations. Our temperature-pressure profiles are computed assuming clear atmospheres and take the spectral properties of several gases into account. The cross-section line lists included are H_2O (Barber et al. 2006), CO_2 (Rothman et al. 2010), CO (Li et al. 2015), CH_4 (Yurchenko & Tennyson 2014), O_2 (Gordon et al. 2017), NO (Wong et al. 2017), SO_2 (Underwood et al. 2016), NH_3 (Yurchenko, Barber & Tennyson 2011), OH (Rothman et al. 2010), HCN (Harris et al. 2006), C_2H_2 (Gordon et al. 2017), PH_3 (Sousa-Silva et al. 2015), H_2S (Azzam et al. 2016), SO_3 (Gordon et al. 2017), PO (Prajapat et al. 2017), SiH (Yurchenko et al. 2018), CaH (Yadin et al. 2012), MgH (Yadin et al. 2012), NaH (Rivlin et al. 2015), AlH (Yurchenko et al. 2018), CrH (Burrows et al. 2002), VO (McK-

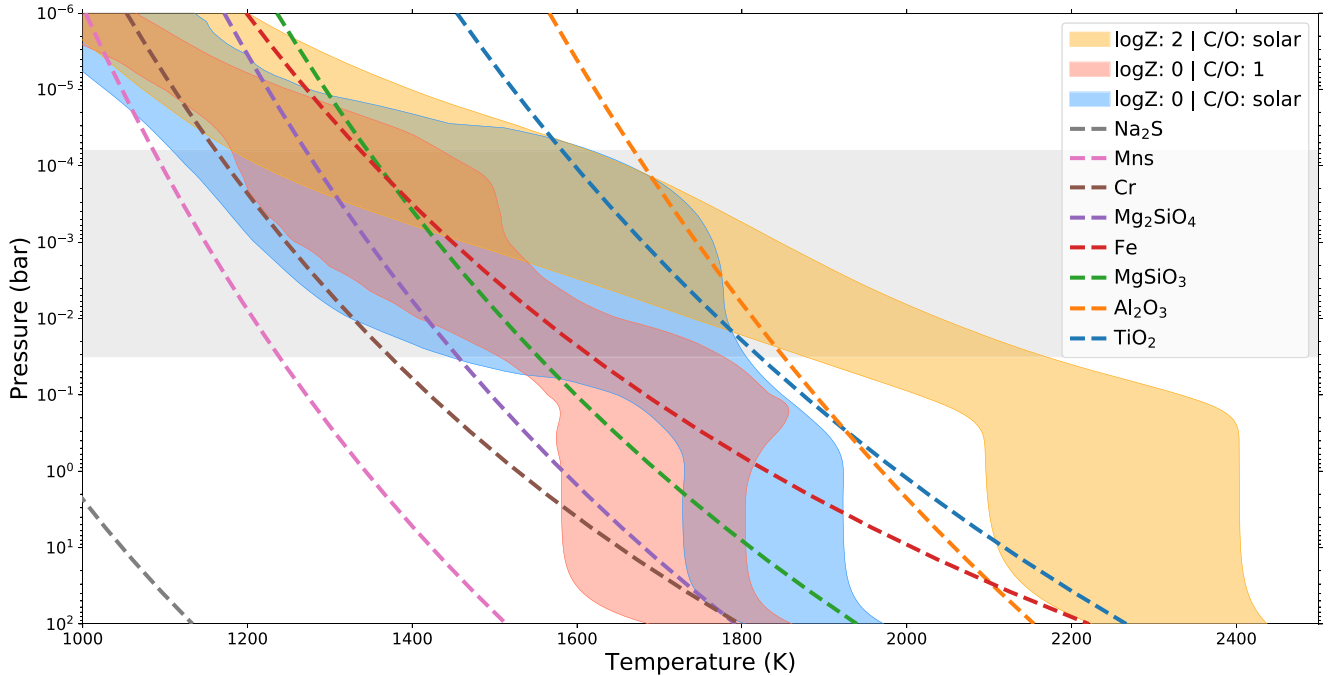


Figure 8. Computed atmospheric T/P profiles under three different assumptions: (1) a solar metallicity and C/O ratio (blue), (2) a solar metallicity and a C/O ratio equal to one (red), and (3) a metal-enriched case with a 100x solar metallicity and a solar C/O ratio (orange). The T/P profiles are indicated by shaded regions where the left-most part assumes a perfect thermal mixing and the right-most part corresponds to the dayside temperature. Also plotted are condensation curves for various cloud-species computed using VIRGA.

emish, Yurchenko & Tennyson 2016), TiO (Ryabchikova et al. 2015), AlO (Patrascu, Yurchenko & Tennyson 2015), SiO (Barton, Yurchenko & Tennyson 2013), CaO (Yurchenko et al. 2016), Na and K (Burrows, Marley & Sharp 2000; Burrows & Volobuyev 2003; Kurucz 2011), H – (John 1988), collision-induced absorption (CIA) H₂–H₂ (Richard et al. 2012), H₂–He (Richard et al. 2012); and scattering cross-sections H₂ (Sneep & Ubachs 2005) and H (Lee & Kim 2004).

In our experiments, the atmosphere is assumed to be in chemical equilibrium, and the concentrations of the gas species are estimated using the open-source code FastChem (Stock et al. 2018). The chemical concentrations computed are then used to build the k -distribution tables for three experiments. The first experiment assumes a 100x solar metallicity and a solar C/O ratio, the second has a solar metallicity and a C/O ratio of unity, and the third has both a solar metallicity and C/O ratio. The experiments are shown in Fig. 8 as shaded regions. The limits to these regions represent the case of perfect heat transport from the dayside to the nightside and the case of no heat transport. The two regimes are obtained by adapting the stellar heating profile in the WASP-101b atmosphere. The adjusted stellar heating rates are computed from the following equation:

$$\frac{dT}{dt}(p)|_{\text{stellar}} = \alpha \int_0^{\pi/2} \frac{dT}{dt}(\theta_z, p) \sin(\theta_z) d\theta_z, \quad (8)$$

where θ_z is the zenith angle, $\frac{dT}{dt}(\theta_z, p)$ is the temperature updates at different pressure levels (p) due to the stellar irradiation at different zenith angles, and α controls the impact of heat transport: 0.5 (perfect heat transport) and 1 (no heat transport). We apply an eight-point Gaussian quadrature integration to solve equation (8). The formulation is similar to the one used in Crisp (1989). In all the experiments, we integrate the model in time until the radiative-convective equilibrium was reached (Malik et al. 2017).

4.2.2 Comparing T/P profiles with cloud profiles

With the T/P profiles in hand, we then compute condensation curves for a range of chemical species that hot Jupiter clouds are contemplated to contain and compare them with the atmospheric T/P profiles. We compute the condensation curves using VIRGA (Rooney, Batalha & Marley 2021). Such a comparison is shown in Fig. 8, where the T/P profiles are plotted as coloured areas and the cloud-particle condensation curves are plotted as dashed lines. Every part of the atmosphere that lies to the left of a condensation curve indicates that cloud formation of that particular species is favoured. Thus, we can rule out Na₂S and MnS clouds in all cases and Cr clouds in the case of a non-Solar C/O ratio and metallicity. However, recent work by Gao et al. (2020) found that planets with equilibrium temperatures $950 \text{ K} < T_{\text{eq}} < 2300 \text{ K}$ have aerosol composition dominated by silicates. Specifically, they predict that at the equilibrium temperature of WASP-101b ($T_{\text{eq}} \sim 1550 \text{ K}$) the aerosol opacity should be dominated by Mg₂SiO₄ (forsterite) with only a very minor contribution from Al₂O₃. While they do not consider MgSiO₃ (enstatite) in their models, which other studies have found should form together with forsterite (Visscher, Lodders & Fegley 2010), the point still stands that the main aerosol contribution should come from silicates. With this in mind and taken together with the compatibility of silicate aerosols with our computed T/P profiles, we speculate that the clouds in WASP-101b are likely to be dominated by silicates.

Interestingly, Garcia Munoz & Isaak (2015) arrived at a similar conclusion for the aerosol composition in Kepler-7b. Kepler-7b has comparable properties ($R = 1.62 R_J$, $M = 0.44 M_J$, $T_{\text{eq}} = 1630 \text{ K}$) to WASP-101b, but is not easily accessible to be probed with transmission spectroscopy ($V = 13 \text{ mag}$). Instead, Garcia Munoz & Isaak (2015) used phase-curve observations combined with the fact that silicate clouds are very reflective leading to a

high geometric albedo to infer the presence of silicate clouds. With different approaches arriving at the same conclusion, we note that this speculation is potentially testable with the Mid-Infrared Instrument (MIRI) on the recently launched *James Webb Space Telescope* (*JWST*) through the major spectral feature from silicate dust around 10 μm (Wakeford & Sing 2015).

4.3 Comparing WASP-101b with the hot Jupiter population

We interpret the optical to NIR transmission spectrum of WASP-101b in the context of the hot Jupiter population that has atmospheric observations. Our results from the 0.3 to 1.7 μm STIS + WFC3 spectrum are in accordance with a high-altitude cloud layer due to the lack of observed spectral features and the overall flatness of the spectrum. Sing et al. (2016) found that hot Jupiters come in a continuum from clear to cloudy and we seek to investigate how our results for WASP-101b fall in this context. Using a sample size of 12 planets, Stevenson (2016) used the strength of the water feature at 1.4 μm as a proxy for cloudiness and found a dividing line in temperature-gravity phase space between cloudy and clear atmospheres. With its equilibrium temperature of ~ 1550 K and a $\log(g) = 2.8$ (cgs), WASP-101b falls close to this divide but does reside in the region proposed to have planets with clear atmospheres. Rather than using the water feature (observed with WFC3) as a proxy for cloudiness, Heng (2016) used observations of the two alkali metals Na and K in the optical (observed with STIS) and found tentative evidence that hotter planets are less likely to be cloudy. With its relatively high equilibrium temperature, WASP-101b does not fit well with this prediction. Expanding the Stevenson (2016) sample to include 37 planets, Fu et al. (2017) did not find a cloudiness dependence on the surface gravity but did reach the same conclusion that planets appear less cloudy with increasing temperature. Again, WASP-101b falls below the proposed correlation between the cloudiness (as measured by the strength of the 1.4 μm water feature) versus the planetary temperature. Interestingly, two other planets (WASP-63b and WASP-17b) with similar equilibrium temperatures (1508 and 1632 K, respectively) also fall well below this line. While this sample size is still too small to say anything significant, it is interesting to consider if unaccounted for physics is responsible for enhancing aerosol production at this temperature. Regardless, these findings at least show that other factors need to be accounted for when considering clouds in the context of hot Jupiters.

5 CONCLUSIONS

We construct the transmission spectrum of the hot Jupiter, WASP-101b, from 0.3 to 1.7 μm . We do this by combining *HST*/STIS observations covering 0.3–1 μm with previously published *HST*/WFC3 observations covering 1.1–1.7 μm . To construct the transmission spectrum, we made use of a Bayesian framework in which we employed the usage of Gaussian processes to model instrumental systematics simultaneously with performing inferences about the planetary atmosphere. We used the analytical transit model of Mandel & Agol (2002) as the mean function of our GP and used a composite kernel function that we found through an evidence-based model comparison. The main conclusion we draw from our results is that the combined transmission spectrum is flat and shows no evidence of absorption features, nor does it show any significant signs of a scattering slope attributed to the presence of hazes. We employed a slightly modified version of the PLATON retrieval code to investigate what information could be extracted from the transmission spectrum and found that the spectrum is best described

by high-altitude aerosols. Indeed, WASP-101b appears to be the cloudiest gas giant observed so far. Clouds are favoured by 3.9σ over a clear atmosphere that is in chemical equilibrium, while clouds are only marginally favoured by 1.7σ over hazes. We investigated what these clouds could be composed of by comparing computed T/P profiles of WASP-101b with condensation curves of a range of hypothesized cloud particles. Though we can only rule out Na_2S and MnS clouds (and Cr clouds in two of the three cases we consider), we speculate that the presence of silicate clouds in the atmosphere of WASP-101b is most likely to be the main contribution to the muted spectral features observed. This speculation can presumably be tested by attempting to observationally detect the strong spectral feature of silicate dust around 10 μm using MIRI aboard *JWST*. Finally, we note that, given the relatively hot equilibrium temperature of WASP-101b, theoretical models do not predict it to be completely clouded. However, this finding is not surprising as other planets that occupy a similar place in parameter space have shown signs of clouds and/or hazes.

ACKNOWLEDGEMENTS

GWH acknowledges that Astronomy at Tennessee State University is supported by the State of Tennessee through its Centers of Excellence Program.

DATA AVAILABILITY

The *HST*/STIS data used in this paper are publicly available in their raw form on the *HST* MAST archive under Cycle 24, GO 14767. The TESS data used are also publicly available at MAST.

REFERENCES

- Ackerman A. S., Marley M. S., 2001, *ApJ*, 556, 872
 Alam M. K. et al., 2021, *ApJ*, 906, L10
 Ambikasaran S., Foreman-Mackey D., Greengard L., Hogg D. W., O’Neil M., 2015, *IEEE Trans. Pattern Anal. Mach. Int.*, 38, 252
 Azzam A. A. A., Tennyson J., Yurchenko S. N., Naumenko O. V., 2016, *MNRAS*, 460, 4063
 Barber R. J., Tennyson J., Harris G. J., Tolchenov R. N., 2006, *MNRAS*, 368, 1087
 Barstow J. K., Aigrain S., Irwin P. G. J., Sing D. K., 2017, *ApJ*, 834, 50
 Barton E. J., Yurchenko S. N., Tennyson J., 2013, *MNRAS*, 434, 1469
 Brown T. M., Charbonneau D., Gilliland R. L., Noyes R. W., Burrows A., 2001, *ApJ*, 552, 699
 Buchner J., 2021, *J. Open Source Softw.*, 6, 3001
 Buchner J. et al., 2014, *A&A*, 564, A125
 Burrows A., Volobuyev M., 2003, *ApJ*, 583, 985
 Burrows A., Marley M. S., Sharp C. M., 2000, *ApJ*, 531, 438
 Burrows A., Ram R. S., Bernath P., Sharp C. M., Milsom J. A., 2002, *ApJ*, 577, 986
 Charbonneau D., Brown T. M., Noyes R. W., Gilliland R. L., 2002, *ApJ*, 568, 377
 Claret A., 2003, *A&A*, 401, 657
 Crisp D., 1989, *Icarus*, 77, 391
 Crossfield I. J. M., Kreidberg L., 2017, *AJ*, 154, 261
 Demory B.-O. et al., 2013, *ApJ*, 776, L25
 Eaton J. A., Henry G. W., Fekel F. C., 2003, in Oswalt T. D., ed., *Astrophysics and Space Science Library* Vol. 288. p. 189
 Evans T. M. et al., 2018, *AJ*, 156, 283
 Feroz F., Hobson M. P., 2008, *MNRAS*, 384, 449
 Feroz F., Hobson M. P., Bridges M., 2009, *MNRAS*, 398, 1601
 Feroz F., Hobson M. P., Cameron E., Pettitt A. N., 2019, *Open J. Astrophys.*, 2, 10

- Fu G., Deming D., Knutson H., Madhusudhan N., Mandell A., Fraine J., 2017, *ApJ*, 847, L22
- Gao P. et al., 2020, *Nat. Astron.*, 4, 951
- Garcia Munoz A., Isaak K. G., 2015, *Proc. Natl. Acad. Sci.*, 112, 13461
- Gibson N. P., Aigrain S., Roberts S., Evans T. M., Osborne M., Pont F., 2012, *MNRAS*, 419, 2683
- Gibson N. P., Aigrain S., Barstow J. K., Evans T. M., Fletcher L. N., Irwin P. G. J., 2013, *MNRAS*, 436, 2974
- Gordon I. E. et al., 2017, *J. Quant. Spec. Radiat. Transf.*, 203, 3
- Goyal J. M., Wakeford H. R., Mayne N. J., Lewis N. K., Drummond B., Sing D. K., 2019, *MNRAS*, 482, 4503
- Harris G. J., Tennyson J., Kaminsky B. M., Pavlenko Y. V., Jones H. R. A., 2006, *MNRAS*, 367, 400
- Hellier C. et al., 2014, *MNRAS*, 440, 1982
- Helling C., Woitke P., Thi W. F., 2008, *A&A*, 485, 547
- Heng K., 2016, *ApJ*, 826, L16
- Henry G. W., 1999, *PASP*, 111, 845
- Huitson C. M., Sing D. K., Vidal-Madjar A., Ballester G. E., Lecavelier des Etangs A., Désert J. M., Pont F., 2012, *MNRAS*, 422, 2477
- Jenkins J. M. et al., 2016, in Chiozzi G., Guzman J. C., eds, Proc. SPIE Conf. Ser. Vol. 9913, Software and Cyberinfrastructure for Astronomy IV. SPIE, Bellingham, p. 99133E
- John T. L., 1988, *A&A*, 193, 189
- Jones D. E., Stenning D. C., Ford E. B., Wolpert R. L., Loredó T. J., Gilbertson C., Dumusque X., 2017, preprint ([arXiv:1711.01318](https://arxiv.org/abs/1711.01318))
- Katsanis R. M., McGrath M. A., 1998, The Calstis IRAF Calibration Tools for STIS Data, Space Telescope STIS Instrument Science Report
- Kreidberg L., 2015, *PASP*, 127, 1161
- Kurucz R. L., 2011, *Can. J. Phys.*, 89, 417
- Lee H.-W., Kim H. I., 2004, *MNRAS*, 347, 802
- Li G., Gordon I. E., Rothman L. S., Tan Y., Hu S.-M., Kassi S., Campargue A., Medvedev E. S., 2015, *ApJS*, 216, 15
- MacDonald R. J., Goyal J. M., Lewis N. K., 2020, *ApJ*, 893, L43
- Malik M. et al., 2017, *AJ*, 153, 56
- Malik M., Kitzmann D., Mendonça J. M., Grimm S. L., Marleau G.-D., Linder E. F., Tsai S.-M., Heng K., 2019, *AJ*, 157, 170
- Mandel K., Agol E., 2002, *ApJ*, 580, L171
- McKemish L. K., Yurchenko S. N., Tennyson J., 2016, *MNRAS*, 463, 771
- Mendonça J. M., Read P. L., Wilson C. F., Lee C., 2015, *Planet. Space Sci.*, 105, 80
- Mendonça J. M., Malik M., Demory B.-O., Heng K., 2018, *AJ*, 155, 150
- Mendonça J. M., Buchhave L. A., 2020, *MNRAS*, 496, 3512
- Nikolov N. et al., 2014, *MNRAS*, 437, 46
- Nikolov N. et al., 2015, *MNRAS*, 447, 463
- Nikolov N. et al., 2018, *Nature*, 557, 526
- Parviainen H., Aigrain S., 2015, *MNRAS*, 453, 3821
- Patrascu A. T., Yurchenko S. N., Tennyson J., 2015, *MNRAS*, 449, 3613
- Pinhas A., Madhusudhan N., Gandhi S., MacDonald R., 2019, *MNRAS*, 482, 1485
- Powell D., Zhang X., Gao P., Parmentier V., 2018, *ApJ*, 860, 18
- Prajapat L., Jagoda P., Lodi L., Gorman M. N., Yurchenko S. N., Tennyson J., 2017, *MNRAS*, 472, 3648
- Rajpaul V., Aigrain S., Osborne M. A., Reece S., Roberts S., 2015, *MNRAS*, 452, 2269
- Rasmussen C. E., Williams C. K. I., 2006, Gaussian Processes for Machine Learning. MIT Press, Cambridge, MA, USA
- Rathcke A. D. et al., 2021, *AJ*, 162, 138
- Richard C. et al., 2012, *J. Quant. Spec. Radiat. Transf.*, 113, 1276
- Rivlin T., Lodi L., Yurchenko S. N., Tennyson J., Le Roy R. J., 2015, *MNRAS*, 451, 634
- Rooney C., Batalha N., Marley M., 2021, in American Astronomical Society Meeting Abstracts. p. 543.06
- Rothman L. S. et al., 2010, *J. Quant. Spec. Radiat. Transf.*, 111, 2139
- Ryabchikova T., Piskunov N., Kurucz R. L., Stempels H. C., Heiter U., Pakhomov Y., Barklem P. S., 2015, *Phys. Scr.*, 90, 054005
- Sing D. K. et al., 2011, *MNRAS*, 416, 1443
- Sing D. K. et al., 2013, *MNRAS*, 436, 2956
- Sing D. K. et al., 2015, *MNRAS*, 446, 2428
- Sing D. K. et al., 2016, *Nature*, 529, 59
- Sneep M., Ubachs W., 2005, *J. Quant. Spec. Radiat. Transf.*, 92, 293
- Sousa-Silva C., Al-Refaie A. F., Tennyson J., Yurchenko S. N., 2015, *MNRAS*, 446, 2337
- Stevenson K. B., 2016, *ApJ*, 817, L16
- Stock J. W., Kitzmann D., Patzer A. B. C., Sedlmayr E., 2018, *MNRAS*, 479, 865
- Tsiaras A. et al., 2018, *AJ*, 155, 156
- Underwood D. S., Tennyson J., Yurchenko S. N., Huang X., Schwenke D. W., Lee T. J., Clausen S., Fateev A., 2016, *MNRAS*, 459, 3890
- Visscher C., Lodders K., Fegley Bruce J., 2010, *ApJ*, 716, 1060
- Wakeford H. R., Sing D. K., 2015, *A&A*, 573, A122
- Wakeford H. R. et al., 2017, *ApJ*, 835, L12
- Wakeford H. R., Wilson T. J., Stevenson K. B., Lewis N. K., 2019, *Res. Notes Am. Astron. Soc.*, 3, 7
- Wong A., Yurchenko S. N., Bernath P., Müller H. S. P., McConkey S., Tennyson J., 2017, *MNRAS*, 470, 882
- Yadin B., Veness T., Conti P., Hill C., Yurchenko S. N., Tennyson J., 2012, *MNRAS*, 425, 34
- Yurchenko S. N., Tennyson J., 2014, *MNRAS*, 440, 1649
- Yurchenko S. N., Barber R. J., Tennyson J., 2011, *MNRAS*, 413, 1828
- Yurchenko S. N., Blissett A., Asari U., Vasilios M., Hill C., Tennyson J., 2016, *MNRAS*, 456, 4524
- Yurchenko S. N., Williams H., Leyland P. C., Lodi L., Tennyson J., 2018, *MNRAS*, 479, 1401
- Zhang M., Chachan Y., Kempton E. M. R., Knutson H. A., Chang W. H., 2020, *ApJ*, 899, 27

APPENDIX

Here, we include tabulated values for the transmission spectrum that is presented in the main text (Table A1).

Table A1. *HST*/STIS broad-band transmission spectrum for WASP-101b together with the used limb-darkening coefficients.

Wavelength range (Å)	R_p/R_*	u_1	u_2	u_3	u_4
2905–3890	0.1095 ± 0.0012	−0.1442	1.0796	−0.0603	−0.0976
3890–4160	0.1095 ± 0.0009	−0.0435	0.4350	1.0150	−0.6323
4160–4370	0.1101 ± 0.0008	−0.1230	0.7619	0.5932	−0.4646
4370–4550	0.1099 ± 0.0008	−0.0330	0.4152	1.0049	−0.6321
4550–4730	0.1104 ± 0.0008	−0.0793	0.6712	0.6262	−0.4770
4730–4920	0.1105 ± 0.0008	−0.1129	0.9301	0.1773	−0.2873
4920–5105	0.1101 ± 0.0008	−0.0565	0.6682	0.4954	−0.4065
5105–5300	0.1101 ± 0.0008	0.0123	0.4235	0.7403	−0.4965
5300–5505	0.1096 ± 0.0008	−0.0230	0.6028	0.4538	−0.3709
5505–5705	0.1097 ± 0.0008	−0.0009	0.5412	0.4922	−0.3842
5260–5650	0.1097 ± 0.0011	−0.0279	0.6381	0.4118	−0.3512
5650–5875	0.1094 ± 0.0010	−0.0956	0.9513	−0.0496	−0.1576
5875–5910	0.1100 ± 0.0024	−0.0930	0.9440	−0.0640	−0.1476
5910–6200	0.1097 ± 0.0010	−0.0979	0.9868	−0.1588	−0.1040
6200–6400	0.1088 ± 0.0010	−0.0997	1.0159	−0.2508	−0.0592
6400–6620	0.1089 ± 0.0010	−0.1288	1.2013	−0.5523	0.0595
6620–6800	0.1088 ± 0.0009	−0.1066	1.0703	−0.3847	0.0008
6800–7050	0.1101 ± 0.0010	−0.1071	1.0790	−0.4258	0.0210
7050–7245	0.1097 ± 0.0010	−0.1069	1.0878	−0.4757	0.0470
7245–7445	0.1094 ± 0.0010	−0.1068	1.0897	−0.5046	0.0622
7445–7600	0.1093 ± 0.0010	−0.1089	1.1030	−0.5379	0.0760
7600–7770	0.1089 ± 0.0011	−0.1100	1.1164	−0.5803	0.0961
7770–8200	0.1093 ± 0.0010	−0.1124	1.1262	−0.6180	0.1131
8200–8650	0.1088 ± 0.0011	−0.1239	1.1946	−0.7723	0.1813
8650–9300	0.1097 ± 0.0011	−0.1186	1.1578	−0.7422	0.1673
9300–10245	0.1097 ± 0.0013	−0.1053	1.0735	−0.6475	0.1319

Notes. Note that these are the results obtained after the stitching correction described in Section 3.4.

This paper has been typeset from a $\text{\TeX}/\text{\LaTeX}$ file prepared by the author.